electronics

MDPI

Article

Piezoelectric MEMS Energy Harvester for Low-Power Applications

George Muscalu [1,2,*], Bogdan Firtat [1], Adrian Anghelescu [1], Carmen Moldovan [1], Silviu Dinulescu [1], Costin Brasoveanu [1], Magdalena Ekwinska [3], Dariusz Szmigiel [3], Michal Zaborowski [3], Jerzy Zajac [3], Ion Stan [4] and Adrian Tulbure [5]

1 National Institute for Research and Development in Microtechnologies, 077190 Bucharest, Romania; bogdan.firtat@imt.ro (B.F.); adrian.anghelescu@imt.ro (A.A.); carmen.moldovan@imt.ro (C.M.); silviu.dinulescu@imt.ro (S.D.); costin.brasoveanu@imt.ro (C.B.)
2 Faculty of Electronics, Telecommunications and Information Technology, University Politehnica of Bucharest, 061071 Bucharest, Romania
3 Sieć Badawcza Łukasiewicz-Instytut Mikroelektroniki i Fotoniki, 02-668 Warszawa, Poland; magdalena.ekwinska@imif.lukasiewicz.gov.pl (M.E.); dariusz.szmigiel@imif.lukasiewicz.gov.pl (D.S.); mzab@ite.waw.pl (M.Z.); jerzy.zajac@imif.lukasiewicz.gov.pl (J.Z.)
4 Romelgen SRL, 021784 Bucharest, Romania; ion.stan@romelgen.ro
5 Department of Informatics, Mathematics and Electronics, University "1 Decembrie1918", 510009 Alba Iulia, Romania; aditulbure@uab.ro
* Correspondence: george.muscalu@imt.ro; Tel.: +40-724-586-932

Abstract: With the global market value of sensors on the rise, this paper focuses on the fabrication and testing of a proof-of-concept piezoelectric energy harvester which is able to harvest mechanical energy from the ambient environment and convert it into electrical energy in order to power wireless sensor networks. We focused on obtaining a new device structure based on a comb-type array of piezoelectric MEMS cantilevers (2 × 10) for a resonant frequency in the environmental application domain (a few hundred Hz) and a chip area of only 1 cm^2. The configuration of the lead-free piezoelectric cantilever consists of a Si substrate, a pair of Ti-Pt electrodes and a sputtered piezoelectric layer of 12% Sc-doped AlN with a thickness of 1000 nm, a dielectric constant of ~13 and $e_{31,f}$ = 1.3 C/m^2. At a resonant frequency of 465.2 Hz and an acceleration of 1 g, the maximum value for the collected power was 2.53 μW for an optimal load resistance of 1 MΩ resulting in a power density of 60.2 nW/mm^3 for the unpacked device, without taking into account the vibration volume. By increasing the excitation acceleration to 2 g RMS and using LTC3588-1 for the power circuitry we were able to obtain a stabilized output voltage of 1.8 V.

Keywords: piezoelectric MEMS; piezoelectric transducer; piezoelectric lead-free material; energy harvester; cantilever array

Citation: Muscalu, G.; Firtat, B.; Anghelescu, A.; Moldovan, C.; Dinulescu, S.; Brasoveanu, C.; Ekwinska, M.; Szmigiel, D.; Zaborowski, M.; Zajac, J.; et al. Piezoelectric MEMS Energy Harvester for Low-Power Applications. *Electronics* **2024**, *13*, 2087. https://doi.org/10.3390/electronics13112087

Academic Editor: Federico Moro

Received: 26 April 2024
Revised: 22 May 2024
Accepted: 22 May 2024
Published: 27 May 2024

1. Introduction

The sensors market is constantly growing and is expected to reach USD 42.1 billion by 2029 for industrial sensors alone [1]. Also, the new strategy of the European Union, the European Green Deal [2], strengthens the growing European interest in a sustainable industry in terms of energy and clean environment. Energy harvesting is the process of collecting a small amount of energy from the environment. It offers a solution to this sustainability problem; by harvesting environmental energy, we should be able to respond to the energy shortage by replacing polluting power supplies, such as batteries, or at least to increase their life span. Another motivation could be the fact that the growing demand for safe, power efficient, and durable systems requiring minimal or no maintenance has resulted in an expanding energy harvesting system market; the value of this market is expected to reach USD 0.9 billion by 2028 [3].

The main energy sources found in the environment are the following: solar, aeolian, acoustic, mechanical vibration, and thermoelectrical. The energy coming from mechanical vibrations could be harvested using four mechanisms: electrostatic, electromagnetic, magneto-strictive, and piezoelectric [4].

In particular, piezoelectric energy harvesters can offer the ability to meet application requirements such as high efficiency in energy conversion and compatibility for miniaturization. Their purpose is to "harvest" mechanical energy, in our case environmental vibrations, which induce strain in the piezoelectric layer, and, due to the direct piezoelectric effect, are converted into electrical energy. One of the best and most-used piezoelectric materials is PZT (lead zirconate titanate) but, in order to be in line with the European strategy, we have to choose a lead-free material for the piezoelectric layer.

Several piezoelectric lead-free materials were taken into account for the fabrication of the energy harvester, such as zinc oxide (ZnO), aluminum nitrate (AlN) or potassium sodium niobate (KNN). ZnO was successfully used by C.T. Pan et al. [5] and Y. Li et al. [6] in developing piezoelectric energy harvesters. Also, I. Kanno et al. [7] and S.S. Won et al. [8] successfully used KNN in developing energy harvesters. However, our preliminary tests have shown that it will be difficult to integrate these materials with our current technological capabilities. Therefore, we focused on using AlN-based piezoelectric materials.

AlN as a piezoelectric film in MEMS energy harvesters has been widely used, as can be seen in [9]. For example, N. Jackson et al. evaluated three different designs of cantilever-based energy harvesters for low frequency usage, using the same piezoelectric film, AlN. They compared a wide beam, trapezoidal beam, and narrow beam structure resulting in a reported power density of 2.5, 0.78, and 0.65 $mW/cm^3/g^2$ at a resonant frequency of 149, 118, and 97 Hz, respectively. The acceleration was 0.2 g for the wide beam and 0.4 g for the other two [10]. The authors also demonstrated an increase in the harvesting bandwidth by using an array of cantilevers. On a 4 cm^2 area, the bandwidth increased from 0.82 Hz to 26.4 Hz for an array of narrow beam cantilevers, from 0.9 Hz to 9 Hz for the trapezoidal ones, and from 1.2 Hz to 4.8 Hz for an array of wide beam cantilevers.

An array of cantilevers was also fabricated by J.-Q. Liu et al. [11]. They used PZT as the piezoelectric material on a silicon cantilever with a nickel-proof mass and obtained an effective electrical power of 3.98 μW. The array consisted of three cantilevers with a resonant frequency between 226 Hz and 234 Hz. In order to overcome the different phases of cantilevers, which could diminish the effect of an array, the authors used a full-bridge rectifier after each cantilever and then connected them together.

Another array of cantilevers was fabricated by H. Yu et al. [12] and X. Zhao et al. [13]. They both used an array of five cantilevers connected together by a common silicon-proof mass. H. Yu used PZT as the piezoelectric material and obtained an output power of 66.75 μW at a resonant frequency of 234.5 Hz and an acceleration of 0.5 g. X. Zhao used AlN as the piezoelectric material and obtained 3.249 μW as the maximum generated power, at a resonant frequency of 230.4 Hz and an acceleration of 1 g.

In terms of improved AlN-based material, a significant increase in the generated energy is obtained by doping the AlN film with scandium (Sc) as S. Barth and others demonstrated [14]. They measured a power of 350 μW for the Sc-doped AlN compared to 70 μW for pure AlN under optimum conditions.

The presented energy harvester consists of a double array of piezoelectric cantilevers fabricated using silicon-based MEMS technologies and Sc-doped AlN as a lead-free piezoelectric material. Sc-doped AlN is compatible with our technological capabilities and it has greater performance over the other materials presented above.

The purpose of the double array of cantilevers (2 × 10) is to obtain a larger output power magnitude for a bandwidth around the resonant frequency. The MEMS device includes 20 piezoelectric cantilevers which are designed as unimorph cantilevers and work in flexure mode with a resonant frequency in the environmental application domain (a few hundred Hz [11]).

Regarding the device topology, we chose narrow beam cantilevers for a better chance of obtaining a bandwidth around the resonant frequency and a smaller area. Although the wide beam cantilever design is more efficient in terms of electrical power, as proven in [15], it could take up a large area, especially when it comes to multiple cantilevers.

The MEMS device was successfully obtained on an area of 1 cm^2. Its resonant frequency is 465.2 Hz (measured with a laser Doppler interferometer) and the cantilevers were connected according to their phases. For an acceleration of 2 g RMS we obtained a stabilized output voltage of 1.8 V at the resonant frequency by using the integrated circuit LTC3588-1. A stabilized voltage of 1.8 V could easily be used to power a wide range of commercially available ultra-low-power microcontrollers, such as STMicroelectronics [16], NXP Semiconductors [17], or Texas Instruments [18], and to intermittently collect data from sensor nodes.

2. Materials and Methods

The energy harvester device described in this paper is based on the direct piezoelectric effect, leading to direct transformation of mechanical energy into electrical energy. When a piezoelectric material is deformed or stressed, a voltage is generated across the material.

The purpose of the research work is to obtain a lead-free energy harvester for supplying inaccessible low-power sensors or sensor networks. It is based on a MEMS device with 20 piezoelectric harvesting cantilevers, designed as unimorph cantilevers working in flexure mode and with the 3–1 transversal mode as the electromechanical coupling mode (the electric field is produced on an axis orthogonally to the axis of applied stress). An overview of one piezoelectric cantilever is presented in Figure 1. The flexure mode is the first mode of vibration and has the lowest resonant frequency. It also provides the largest deflection and therefore the largest amount of electrical energy. Adding a proof mass will further lower the resonant frequency to a resonant frequency closer to the physical vibration sources.

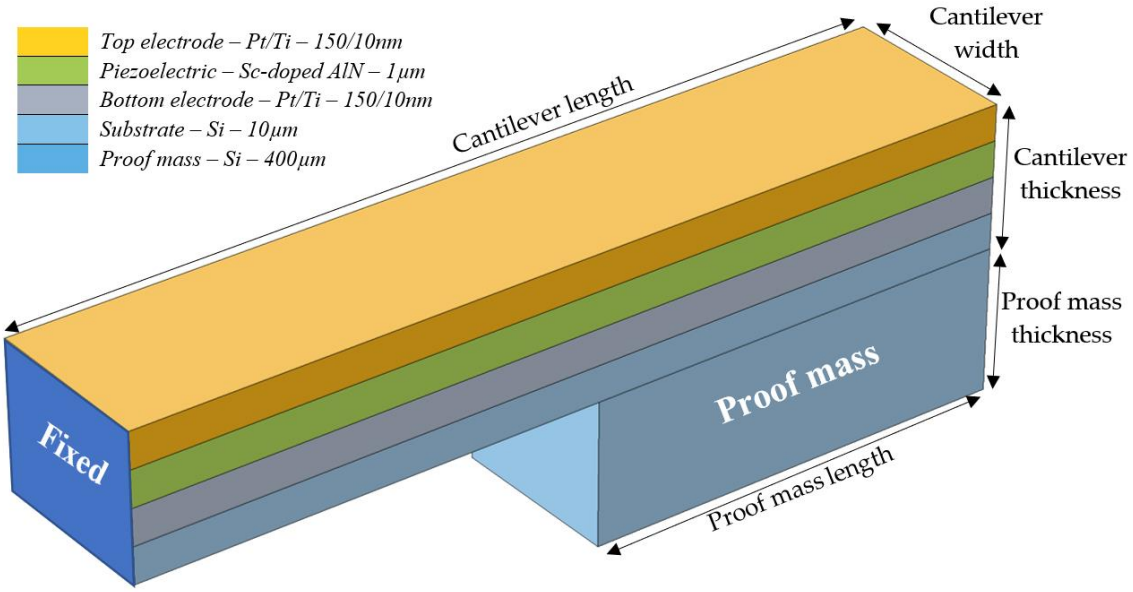

Figure 1. Overview of the piezoelectric cantilever.

Several lead-free piezoelectric materials were studied for the device fabrication, such as KNN, nanostructured ZnO, AlN, and Sc-doped AlN. Due to the incompatibility of the KNN and nanostructured ZnO fabrication steps with our technology capabilities, we were unable to integrate these piezoelectric materials with our device. Between AlN and Sc-

doped AlN we chose the latter because of its superior piezoelectric properties over the AlN [10] and its very good compatibility with the silicon technology.

We focused on obtaining a double array of proof mass cantilevers for a resonant frequency in the environmental application domain (a few hundred Hz) and a chip area of only 1 cm^2. An array of cantilevers could provide us with a bandwidth of frequencies from which we could collect energy from the environment but with the cost of power magnitude. Also, this design gives us the possibility to connect multiple cantilevers in a small area.

The resonant frequency could be described by the equation below, assuming the added mass on the tip is much larger than the mass of the beam itself and the stiffness is unaffected [19]:

$$f = \frac{1}{2\pi}\sqrt{\frac{Y_{eq}Wt^3}{4L^3(m_i + 0.24m_c)}} \quad (1)$$

where Y_{eq} is the equivalent Young's modulus, t, L and W are the thickness, length and width of the cantilever beam and m_i and m_c are the mass of the proof mass and the cantilever mass, respectively. As can be seen, the resonant frequency is given by the materials' properties and the geometric parameters. Once the materials are set, the geometric parameters (length, thickness, and proof mass) are used in order to tune the resonant frequency.

The chosen software for employing the finite element method (FEM) was COMSOL Multiphysics 5.2, out of several similar tools available to us, including Ansys 18.1 and CoventorWare 2014, which can provide similar results. The reasons for choosing this software lie both in the team's greater experience with COMSOL and several key attributes. On the one hand, CoventorWare is an excellent simulation tool when used in conjunction with microfabrication technologies. Ansys, on the other hand, is an excellent FEM tool for engineering applications, offering a broad suite of software products that cover various engineering disciplines. However, COMSOL, focused on multiphysics simulations, is usually the main choice for academic applications, due to its seamless capabilities to simulate coupled phenomena.

Regarding the current modeling and simulation purpose, our intention was to analyze the physical behavior, to determine the main outputs and to maximize the device's efficiency through optimization. COMSOL's meshing options provided the authors with better options to integrate very high geometrical aspect ratios (the length of the cantilever is in the millimeter range, while the thickness of the metal layers only has a few hundred nanometers) without high computational costs.

The simulation consists of a modal analysis for the eigenfrequencies, in order to determine the resonant frequency for the cantilever. The geometric parameters are as follows: a cantilever length of 2500 μm; a proof mass length of 1200 μm; a width of 300 μm for both parts, the cantilever and the proof mass; and a cantilever thickness of 10 μm. The thickness of the proof mass is 400 μm, the same as the thickness of the wafer. We obtained a resonant frequency for the first vibration mode (flexure mode) of around 460 Hz, as can be seen in Figure 2a. For the simulation we used the materials described by Figure 1, with their properties from the COMSOL library. We also took into account the effects of the DRIE process from the process flow resulting in a slightly larger proof mass (a width of 340 μm and a length of 1220 μm). The mesh consists of 61,487 domain elements, 23,042 boundary elements, and 1926 edge elements (Figure 2b).

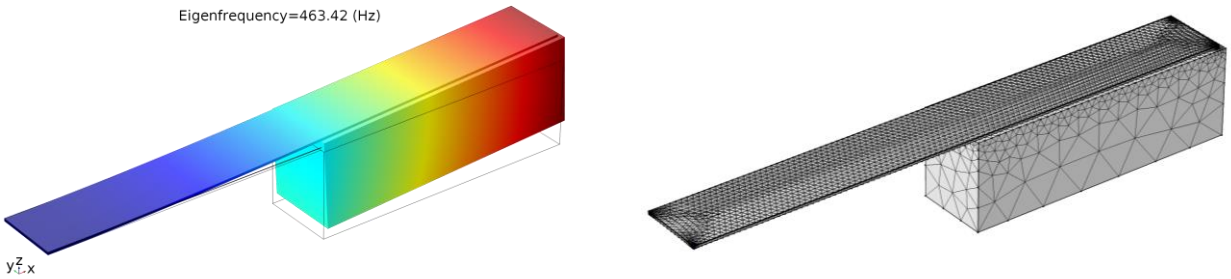

(**a**) (**b**)

Figure 2. (**a**) The first vibration mode (flexure mode) for the piezoelectric cantilever; (**b**) the mesh for the simulated structure.

Using the geometric parameters from the simulation, we designed the fabrication masks (Figure 3) and the process flow (Figure 4). The process flow consists of five masks and deploys MEMS technologies for the fabrication of the energy harvester. It was designed for using only positive photoresists. The masks and process flow were fabricated by IMT-Bucharest, through IMT-MINAFAB, except for the piezoelectric layer which was provided by PIEMACS Sàrl (Lausanne, Switzerland).

The process starts with a SOI (silicon on insulator) wafer (device thickness of 10 µm, buried oxide of 500 nm and handler thickness of 400 µm) on which we thermally grew a silicon oxide layer of 500 nm. On top of the wafer, we deposited Ti-Pt (10–150 nm) by evaporation and patterned it by lift-off, resulting in the bottom electrode (Figure 4a), using Mask 1 (Figure 3a).

The next step is the deposition of the piezoelectric layer by RF sputtering (Figure 4b) and its patterning using Mask 2 (Figure 3b). The piezoelectric layer is 12% Sc-doped AlN and was possible thanks to PIEMACS Sàrl. The relative dielectric constant of the piezoelectric material is around 13 and its piezoelectric coefficient is around $e_{31,f}$ = 1.3 C/m² [20]. Also, the dielectric loss did not increase with Sc doping [20].

The *Figure of Merit (FOM)* could be described by the following equation [21]:

$$FOM = \frac{d_{31}^2}{\varepsilon \cdot tan\delta} \quad (2)$$

The piezoelectric coefficient d_{31} is determined using the known relation [22]:

$$e_{31} = \frac{d_{31}}{s_{11} + s_{12}} \quad (3)$$

Equation (3) could be simplified as s_{12} is negligible and hence we obtain the following:

$$e_{31} = d_{31} \cdot Y \quad (4)$$

where Y is the Young's modulus.

With a value of 150 GPa for Young's modulus at a concentration of 12% for Sc [14], we determine $\boldsymbol{d_{31} = 8.3}$ and a ***FOM of 52.6*** (dielectric loss 0.1).

The top electrode (Figure 4c) is deposited as Ti-Pt (10–150 nm) by evaporation and patterned by lift-off using Mask 3 (Figure 3c).

Mask 4 (Figure 3d) is used to configure the cantilevers in the device layer of the SOI wafer by etching the silicon with a Bosch process of a deep reactive ion etching (DRIE) as shown in Figure 4d.

The last step is to release the cantilevers by etching the back of the wafer using Mask 5 (Figure 3e) and DRIE. The DRIE etch is stopped on the buried oxide layer. Afterwards, the buried oxide is etched using wet etching in a buffered hydrofluoric acid (BHF) solution and therefore the cantilevers are fully released (Figure 4e). The distance between the cantilevers was designed at 300 µm to guarantee the silicon etching between the proof masses.

The DRIE process depends on the geometry of the mask. For small etching windows, like the space between the proof masses of the cantilevers, the etch rate is much lower than

for big open etching windows, like near the base of the cantilevers, and the cantilevers will be fixed together. In order to make the etch rate uniform, we introduced some sacrificial structures between the cantilevers, as shown in Figure 3e. These sacrificial structures were removed with the etching of the buried oxide. The overlayed masks are shown in Figure 3f.

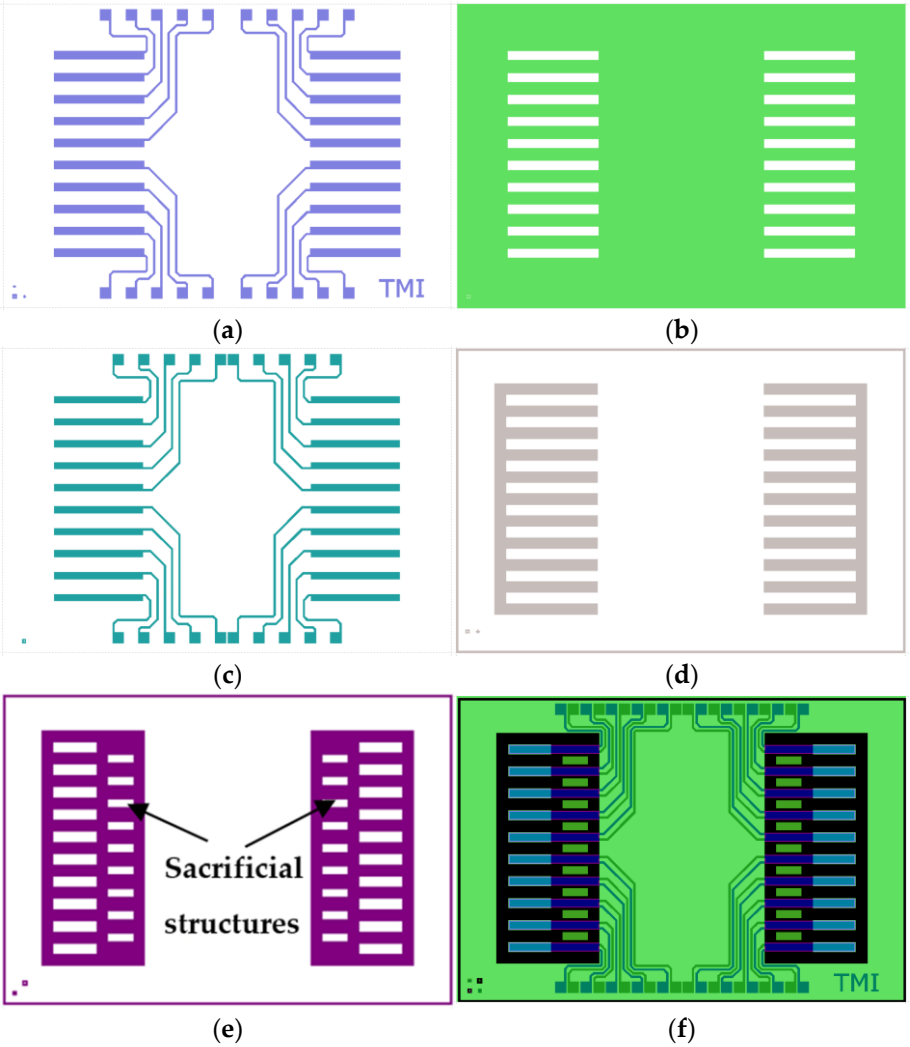

Figure 3. The process masks for one MEMS device: (**a**) Mask 1—bottom electrode patterning; (**b**) Mask 2—piezoelectric configuration; (**c**) Mask 3—top electrode patterning; (**d**) Mask 4—cantilevers configuration; (**e**) Mask 5—cantilevers release; (**f**) overlaying of the five masks.

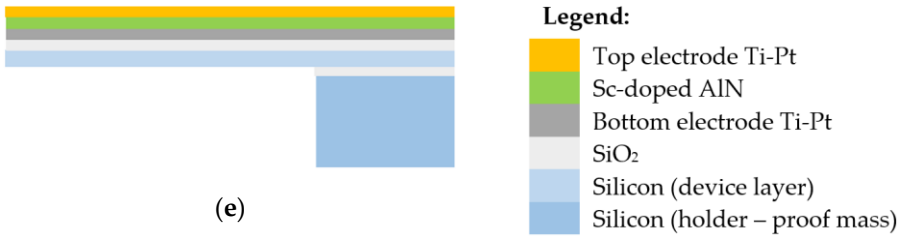

Figure 4. Process flow: (**a**) metal deposition and patterning (bottom electrode); (**b**) piezoelectric deposition and configuration; (**c**) metal deposition and pattering (top electrode); (**d**) cantilevers configuration on the front of the wafer; (**e**) structures release.

3. Results

3.1. Device Fabrication

Following the steps described in the previous section, we obtained several silicon die structures for our prototype harvester (PZ-EH). One such die structure has an **area of 1.02 cm²**. Further on, this die is fixed onto a custom-design ceramic package, with wire bonds connecting from die contact pads to the external pins on the ceramic package (illustrated in Figure 5a), which is finally soldered onto a test printed circuit board (PCB) (illustrated in Figure 5b). These steps facilitate easy access to each individual cantilever's electrical output, for measurements in evaluation and characterization, which we will discuss next. The ceramic packaging for PZ-EH was provided by HIPOT-RR (Otocec, Slovenia). It was made using low-temperature co-fired ceramic (LTCC) and is described in [23]. It also has a lid which we did not use for this step in the project.

For identification purposes, we visually partitioned the piezoelectric die chip cantilevers into four quadrants with five cantilevers each and labeled the cantilevers with numbers starting from the left edge of each quadrant (Figure 5a).

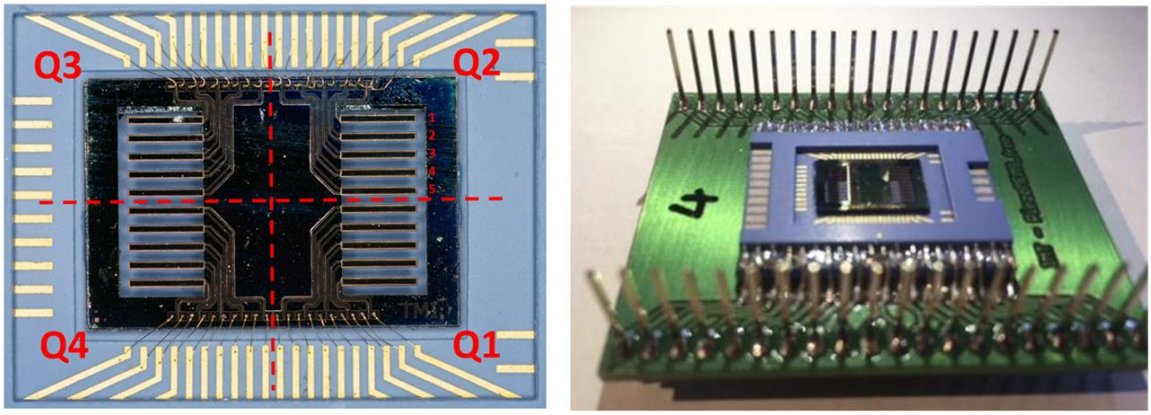

(**a**) (**b**)

Figure 5. (**a**) PZ-EH fixed on ceramic packaging; (**b**) PZ-EH ready for measurements.

3.2. Frequency and Phase Measurements

The resonant frequency, f, of the piezoelectric cantilevers was measured using a Doppler interferometer-based vibration analyzer system, MSA-500 from Polytec (Irvine, CA, USA). A test structure sample is placed under mechanical excitation and the resonant frequency is detected using a laser beam shined on the tip of the cantilever, as shown in Figure 6. This type of measurement offers information about the phase, φ, and the quality factor, Q, too. The results are presented in Table 1.

Table 1. Doppler interferometer results.

Quadrant	Cantilever														
	1			2			3			4			5		
	f [Hz]	Q	φ [°]	f [Hz]	Q	φ [°]	f [Hz]	Q	φ [°]	f [Hz]	Q	φ [°]	f [Hz]	Q	φ [°]
1	465.4	1751	-	465.3	2028	19.34	464.8	1909	32.47	465.3	1854	19.21	456.2	1824	23.12
2	462.2	1383	19.33	464.6	1423	23.01	468.3	2397	21.56	468	1357	27.7	463.4	2069	32.46
3	462.3	1782	21.48	475.2	930	N/A	482.2	820	44.1	463.6	1865	57.49	463.7	1735	N/A
4	464.2	N/A	4.63	476.1	1915	18.41	464.1	1600	20.89	464	1634	19.51	461.7	1790	10.84

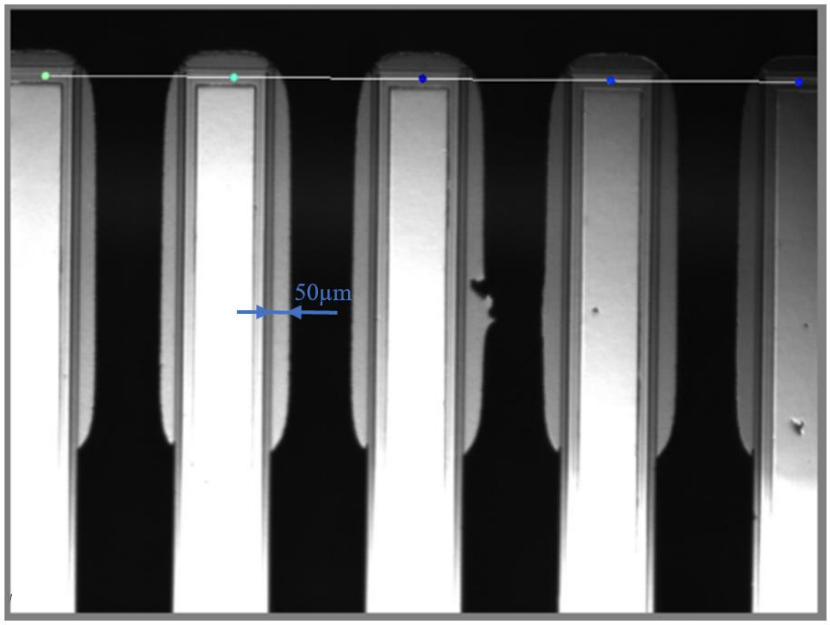

Figure 6. An array of five cantilevers during frequency measurements.

One observation from these measurements pertains to the variance in the relative phase between the incident and the reflected optical signal phases measured for each cantilever. The reference phase for the cantilevers was chosen to be the phase of the first one (cantilever 1 from quadrant 1). From the phase data given in Table 1 we can see that, within the same die, there is a relative phase mismatch between each of the 20 individual cantilevers. The mismatch is the sum of the multiple parameter variances within the die area of approximately 1 cm^2. The results from this characterization step make it easier to identify cantilevers with similar phases in order to optimally connect them together. Another observation pertains to the high Q factor (~2000), which implies the fact that the cantilever structures are highly selective in frequency. This could be a disadvantage since it makes it easier to lose environmental energy, should the frequency of the vibration not match the individual resonant frequency. However, if the vibration and resonant frequencies match, the given electrical output level is higher, which in return allows a more efficient interconnection of the cantilever structures. This could lead to an overall greater harvesting efficiency with the same number of cantilever structures on one die chip.

Due to our DRIE process for releasing the cantilever structures (Figure 4e), the proof mass is slightly larger than intended, as seen in Figure 6. We took these effects into consideration for the simulation presented in Figure 2.

3.3. Experimental Setup for Measurements

The electrical measurements were made using the experimental setup described in Figure 7. This setup serves to provide a known and controlled mechanical excitation to

the DUT, for characterizing our PZ-EH devices. A function generator allows us to fine tune the resonant frequency of the device with the help of the audio amplifier and the audio speaker. For the audio speaker, we used a Somogyi Audio Line SRP1010 woofer (50 W, 8Ω) and it was calibrated with a ~20 grams load (equivalent mass of the encapsulated MEMS and accelerometer) using a commercial system. Independently to the calibration, we also measured the acceleration using a 820M1 single-axis condition-monitoring accelerometer from TE connectivity [24]. The connections between the encapsulated device (presented in Figure 5b) and the additional electronics circuitry are made using a breadboard. The signals' waveforms are monitored using an oscilloscope.

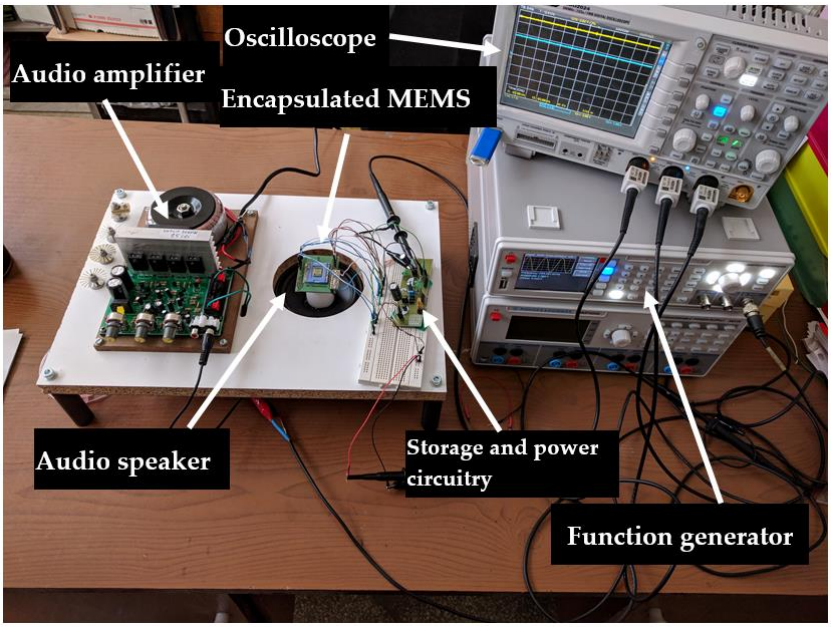

Figure 7. Experimental setup for the testing of the developed PZ-EH device together with additional electronics circuitry.

3.4. Device Characterization

As mentioned in the previous paragraph, we designed the die chip to contain 20 individual cantilever structures; however, the interconnections between the structures have been left outside the die, for reasons which we will detail further. The electrical outputs of each individual cantilever structure can be interconnected either in series, parallel, or a combination of both, in order to maximize the total harvested energy, and also account for the minimum input voltage level requirements of the DC-DC Buck in the LTC3588. A more detailed investigation regarding this aspect has been discussed in [25].

Because of some variations in the technological process and amplified by their high Q factor, it was not possible to efficiently connect all the 20 cantilevers. Therefore, only 10 cantilevers with similar phases were grouped together in order to increase the output power. Otherwise, the signal would be heavily reduced. The 10 cantilevers were chosen according to their phases from Table 1. Table 2 shows the 10 cantilevers together with their phases and their RMS voltage response at an excitation of 1 g. The blank cells correspond to the cantilevers which were left unconnected.

An array of cantilevers could provide us with a bandwidth of frequencies out of which we could collect energy from the environment. *The 10 connected cantilevers (Table 2) were* grouped in 2 branches in series, with 5 cantilevers in parallel in each group (5p2s group). *The array can be described as follows: the 1st branch is composed of cantilever 1 from quadrant 1 (C11) in parallel with cantilever 2 from quadrant 1 (C12) in parallel with cantilever 3 from quadrant 1 (C13) in parallel with cantilever 4 from quadrant 1 (C14) in parallel with cantilever 2 from quadrant 4 (C42), in series with the 2nd branch composed of cantilever 1 from*

quadrant 2 (C21) in parallel with cantilever 2 from quadrant 2 (C22) in parallel with cantilever 3 from quadrant 2 (C23) in parallel with cantilever 4 from quadrant 2 (C24) in parallel with cantilever 1 from quadrant 3 (C31). Grouping the 10 cantilevers resulted in an increased bandwidth of the response, as shown in Figure 8. The excitation acceleration was 1 g and the measurements were made using the oscilloscope probes, without connecting the cantilevers or the 5p2s group to the additional electronics. The uncertainty for the peak-to-peak amplitude measurements was below 5% and for the frequency measurements, it was below 1 Hz. This design gives us the possibility to connect multiple cantilevers in a small area.

Table 2. Electrical measurements at resonant frequency and a = 1 g for the connected cantilevers; the blank gray cells represent the unconnected cantilevers.

Quadrant	Cantilever														
	1			2			3			4			5		
	f [Hz]	V_{RMS} [V]	φ [°]	f [Hz]	V_{RMS} [V]	φ [°]	f [Hz]	V_{RMS} [V]	φ [°]	f [Hz]	V_{RMS} [V]	φ [°]	f [Hz]	V_{RMS} [V]	φ [°]
1	465.4	0.46	-	465.3	1.36	19.34	464.8	1.84	32.47	465.3	2.08	19.21			
2	462.2	1.28	19.33	464.6	1.28	23.01	468.3	0.85	21.56	468	1.2	27.7			
3	462.3	1.15	21.48												
4				476.1	2.4	18.41									

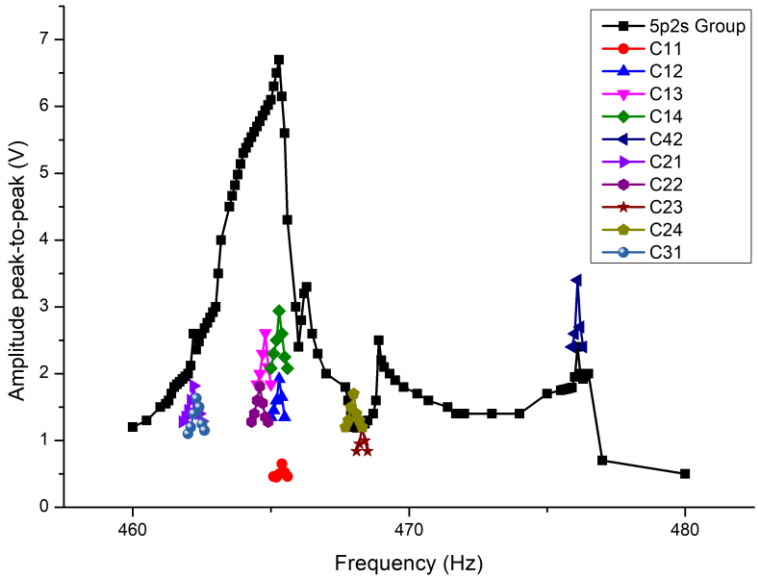

Figure 8. The 5p2s grouping compared to its component cantilevers (1 g acceleration), without additional electronics.

The 5p2s group's performance, relative to the applied test's vibration acceleration, is shown in Figure 9. The measurements were made at a resonant frequency of 465.2 Hz, with the 5p2s group's electrical output being loaded only by the oscilloscope probe (10 MΩ, 8 pF). The response amplitude shows substantial increases at 0.8 g and 1.7 g. A possible explanation is a slight shift (+/−1 Hz) in acceleration for the resonant frequencies or phases from the component cantilevers, resulting in a better matching for the overall grouping.

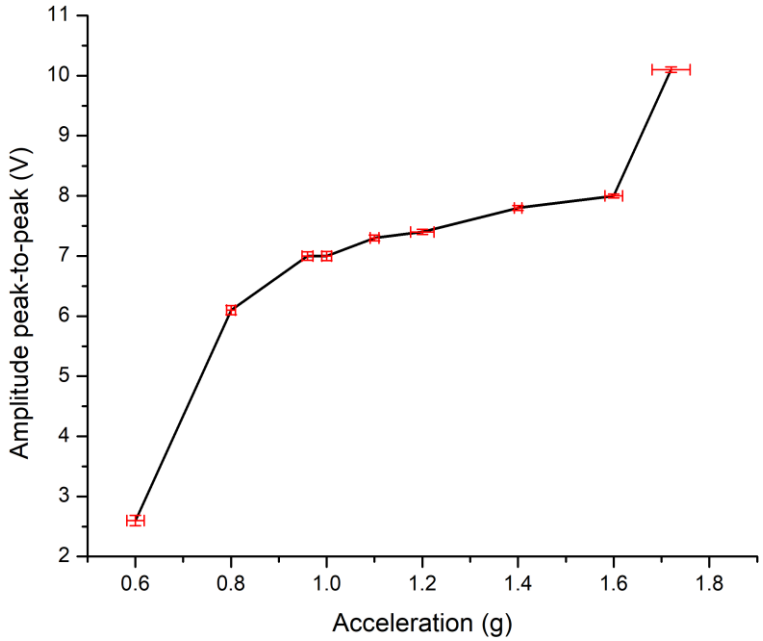

Figure 9. The 5p2s group's peak-to-peak amplitude relative to acceleration, without additional electronics.

Next, we move on to measure the 5p2s group's performance, at different electrical loads (tolerance of 0.01%); the results are illustrated in the following two graphs, shown in Figure 10 and Figure 11, respectively. The mechanical excitation was performed at 465.3 Hz (resonant frequency of the grouping) and an acceleration of 1 g. The impedance of the oscilloscope probes was taken into consideration for these representations. The plot in Figure 10 shows the peak-to-peak amplitude of the grouping versus a few discrete resistive load values, and in Figure 11 its calculated power is shown. The maximum value for the collected power was 2.53 μW for an optimal load resistance of 1 MΩ. In this case, the normalized power density of the device is 0.215 $\mu W/mm^3/g^2$, for the unpacked device without the vibration volume.

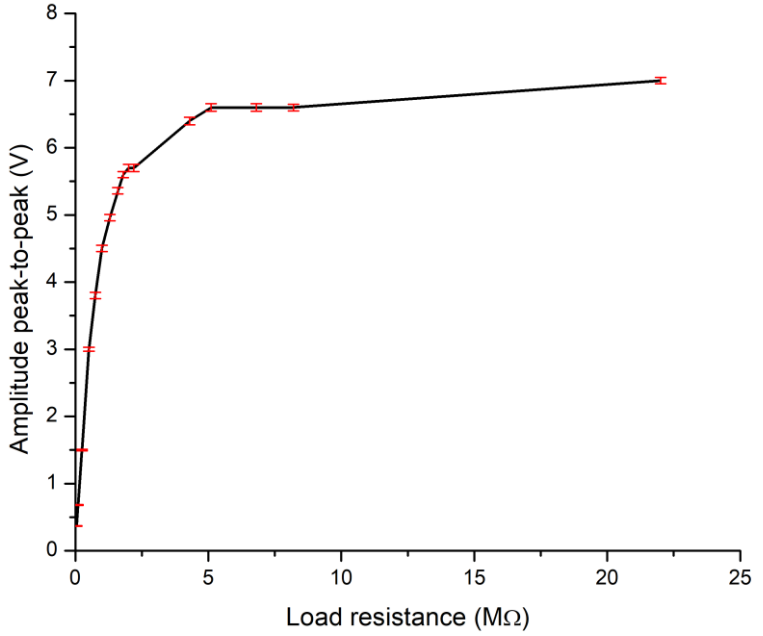

Figure 10. The 5p2s group's peak-to-peak amplitude relative to the load resistance, without additional electronics.

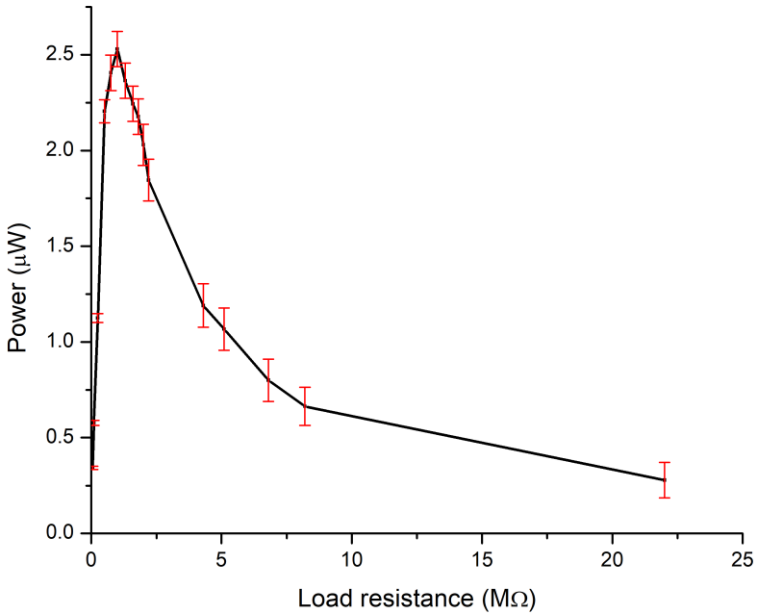

Figure 11. The 5p2s group's power relative to the load resistance, without additional electronics.

3.5. Conversion Circuit

For the voltage conversion circuitry, we used a solution based on a commercially available DC-DC converter IC (integrated circuit), Analog Devices' (formerly Linear Technologies') LTC3588-1 Buck converter, since this chip conveniently integrates a low-loss full-wave bridge rectifier, along with a highly efficient switching Buck converter, optimized for low-power applications, in order to obtain a regulated, useful output voltage level for powering the targeted applications. Figure 12 illustrates the schematic for the entire power harvesting, conversion, and storage circuit we used in some of our tests. Here, our packaged PZ-EH device is electrically tied to the PZ1 and PZ2 inputs of the IC chip, thus effectively using the on-board bridge rectifier, in order to convert from piezo AC output voltage to rectified DC voltage. An intermediary capacitor, C1, placed between the bridge rectifier and converter, allows the accumulation of energy. When the voltage level that is building up between the terminals of C1 reaches a certain threshold level, the DC-DC switching circuitry is effectively turned on and energy is allowed to be transferred to the output on the capacitor C4 [26]. A digital '1' or '0' voltage level selection on pins D0 and D1 allow the user to set the regulated output voltage to a useful level, according to the specifications given by the target application. From the sole standpoint of our converter circuit, lower values for the input and output capacitors (C1 and C4) allow a quick testing of the device. A larger value will take a lot more time to charge but it is more appropriate for a low-power application as we demonstrated in [25]. The L1, C2, and C3 values are given by the datasheet and Pgood is logic "1" when the output signal is stabilized and ready to be used. LTC3588-1 offers the possibility of four output voltages (1.8 V, 2.5 V, 3.3 V, 3.6 V) but we chose 1.8 V for our application because it is a voltage level that allows us to supply commercial ultra-low-power microcontrollers [16–18].

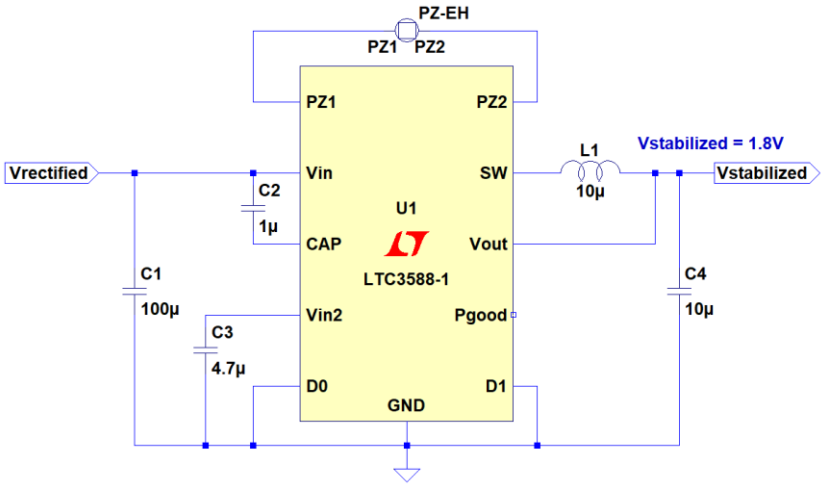

Figure 12. Electrical schematic for the conversion circuit using LTC3588-1.

3.6. Device Characterization with the Conversion Circuit

The target for the fabrication of this device was to obtain a useful stabilized voltage. For this, we used the circuit described in sub-paragraph 3.5 and Figure 12, under 'no load' conditions (except oscilloscope probe loading) and using only the oscilloscope probes for measurements.

At an acceleration of ~1 g, the 5p2s group's open load peak-to-peak amplitude is 5.52 V (Figure 13a). When we connect the device to the storage and power circuit, between PZ1 and PZ2 (Figure 12), the peak-to-peak amplitude drops to 3.8 V (Figure 13b). Therefore, we had to increase the acceleration in order to compensate for this drop-off. At an acceleration of ~1.5 g, the 5p2s group's peak-to-peak amplitude is 11.20 V which drops to 8.72 V when we connect it to the circuit (Figure 13c,d). Even though the value of 8.72 V was enough to start the power circuitry, we had to increase the acceleration even further to reach a stabilized voltage of 1.8 V.

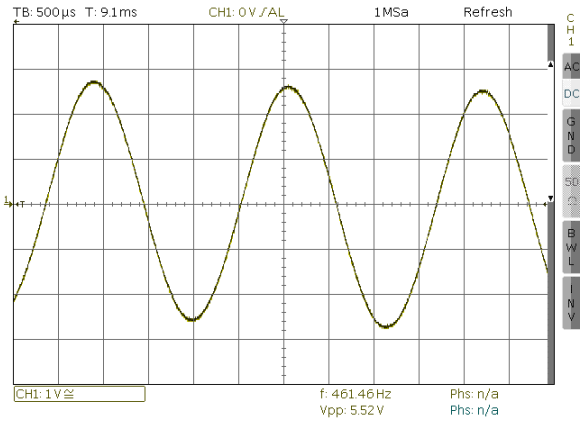

(**a**) Acceleration of 1 g, without the conversion circuit

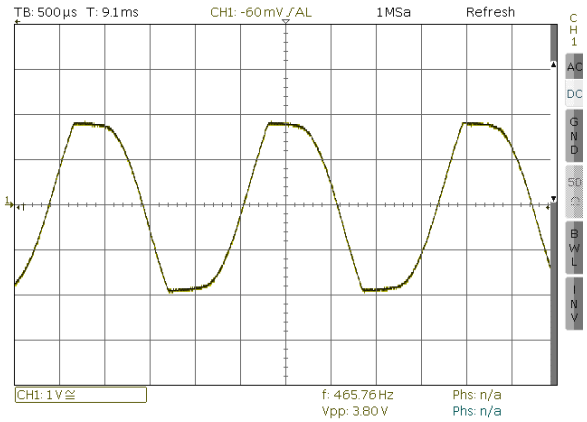

(**b**) Acceleration of 1 g, with the conversion circuit

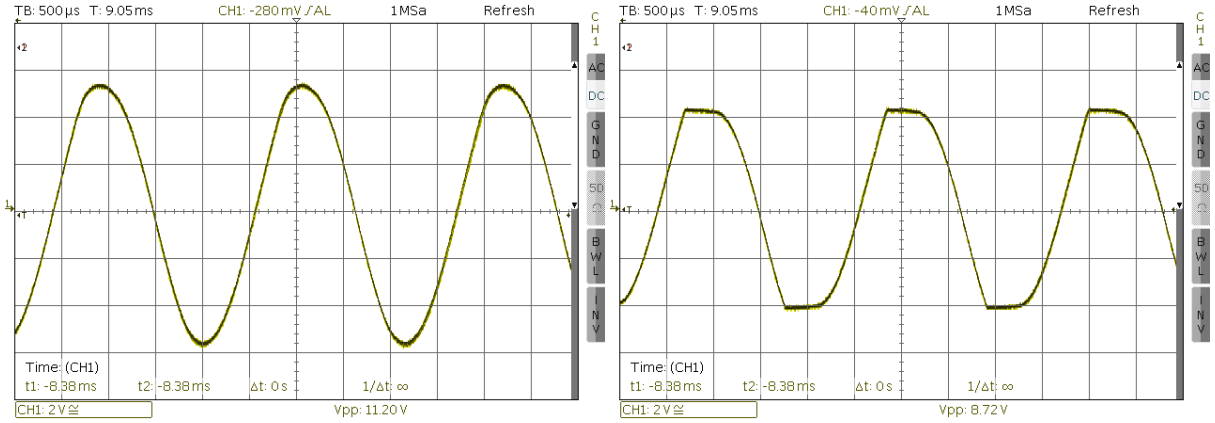

(**c**) Acceleration of 5 g, without the conversion circuit

(**d**) Acceleration of 1.5 g, with the conversion circuit

Figure 13. The 5p2s group at an acceleration of 1 g (**a**,**b**) and 1.5 g (**c**,**d**), measured between PZ1 and PZ2.

By increasing the acceleration to 2 g RMS, the 5p2s group was able to generate a voltage close to 15 V peak to peak (Figure 14). When connected to the conversion circuit, the signal passes through an internal full-wave bridge rectifier and the rectified output is stored on the input capacitor, C1, at the Vin pin. The charging curve for the input capacitor is shown in Figure 15a. In this case, C1 starts charging from point A up to the undervoltage lockout threshold, a typical value of 4.04 V (point B), in around 374 s. When it reaches this value, the internal Buck converter is enabled and the charge is transferred from the input capacitor to the output capacitor, hence the drop to point C. The cycle repeats until a stabilized voltage is reached on the Vout pin. At this acceleration, 2 g RMS, and an excitation frequency of 465.3 Hz, we obtained a stabilized output voltage of 1.8 V, measured on the Vout pin, as it can be seen on the oscilloscope in Figure 7 and detailed in Figure 15b. For the capacitors' values from Figure 12 we needed 12 min to reach an output voltage of 1.8 V.

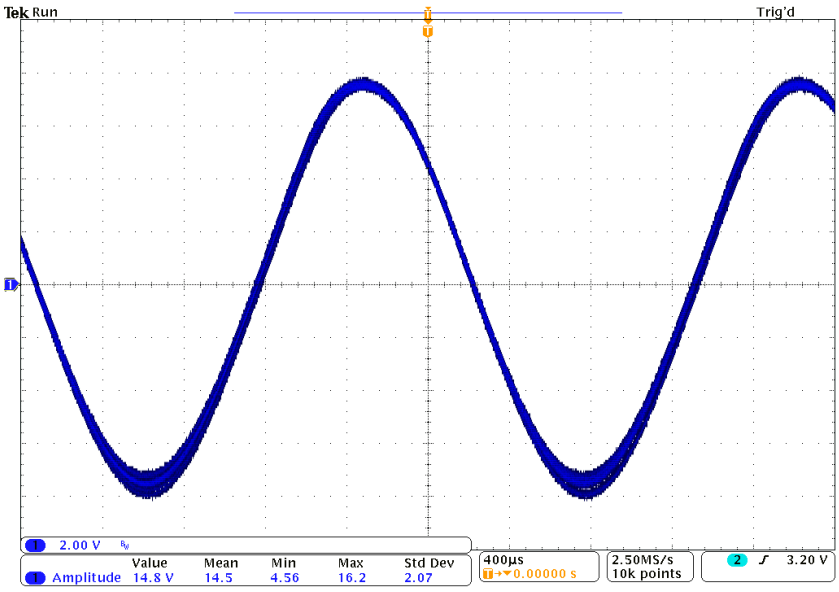

Figure 14. The 5p2s group at an acceleration of 2 g, without the conversion circuit.

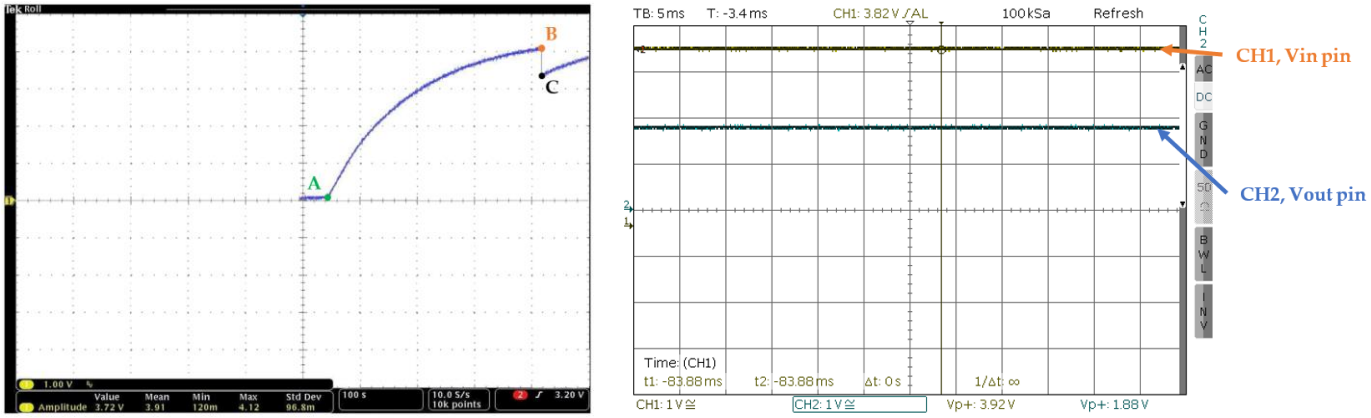

(**a**) (**b**)

Figure 15. (**a**) The charging curve for the input capacitor, C1, 1 V/div and 100 s/div: point A – start charging, point B – threshold voltage and transfer to the output capacitor, point C – start charging again; (**b**) the oscilloscope capture for a stabilized output voltage of 1.8 V on the Vout pin.

4. Discussion

The piezoelectrical MEMS energy harvester with 2 × 10 piezoelectric cantilevers array was successfully fabricated and tested, and the resulting resonant frequency was ~465 Hz. The chip area was 1.02 cm^2.

Sc-doped AlN has been chosen as the piezoelectric material because of its high performance and good compatibility with silicon-based technologies.

For the conversion circuit we chose the integrated circuit LTC3588-1, an off-the-shelf solution which is capable of offering various stabilized voltages, including 1.8 V. An experimental setup was built in order to test the MEMS devices at the desired frequencies, a setup which consists of a function generator, an oscilloscope, an audio amplifier, and a speaker.

We obtained a stabilized output of 1.8 V at a resonant frequency of 465.2 Hz and an acceleration of 2 g RMS. The resonant frequency of 465.2 Hz is not for one cantilever but for the whole group, in this case, two branches in series with five cantilevers in parallel each.

The purpose of the cantilever array was to increase the frequency bandwidth from which we collect the ambient energy and, at the same time, to multiply the collected signal. We observed an improvement in the frequency bandwidth from which the device harvests the energy. This improvement was smaller than expected due to the unforeseen high values for the Q factor and the difficulty in phase-matching the cantilevers.

A challenge in the fabrication processes was the backside etching, etching which has to be performed through the whole wafer in order to configurate the proof masses of the cantilevers. It can be seen visually in Figure 6, as well as in the measurements from Table 1, that the etching process needs further optimization because of its variation, variation which can be observed in the small differences between the resonant frequencies and phases of the cantilevers. This variation is a drawback for the efficiency of the device because we could not use all the cantilevers from the same chip and we had to work with only half, connected together in 2 branches in series of 10 cantilevers in parallel each.

By itself, the device is capable of generating a power of 2.53 μW for an optimal load resistance of 1 MΩ, at an excitation of 1 g and a resonant frequency of 465.3 Hz. In this case, the normalized power density of the device is 0.215 $\mu W/mm^3/g^2$, for the unpacked device without the vibration volume. In order to take advantage of this, we would need to match this load resistance with the input impedance of the power circuitry which was not possible at this stage.

Comparing our device with others could be pretty difficult, as there are different designs, employment of different material or other factors. A common comparison factor is

the power density normalized against acceleration squared, which includes information about the output power at an optimal resistance, at the resonant frequency, as well as the acceleration and the volume of the device. Ideally, the volume of the device should include the volume of the resonator (the cantilever, for example), the volume of the additional elements (like spacing, traces, or frame for manipulation) and the displacement volume during operation. However, due to insufficient information on this matter, it is impossible to centralize this type of information. Therefore, in the calculus of the normalized power density, we only took into consideration the volume of the resonant structure(s), including the design elements like spacing between cantilevers. As the length of the structure, we considered the overall length (cantilever beam and proof mass); as the width of the structure, we considered the maximum width (in case of trapezoidal or tennis racket cantilevers); and as thickness, we considered the sum of all the layers. These results are shown in Table 3.

Table 3. Comparison of the harvester device with the literature.

Device	Material	Dimension (mm^3)	Resonant Frequency (Hz)	Acceleration (g)	Optimal Resistance (kΩ)	Q-Factor	$Power_{max}$ (μW)	Power Density ($\mu W \cdot mm^{-3} \cdot g^{-2}$)
PZ-EH	ScAlN	2 × (2.5 × 5.7 × 0.412)	465.3	1	1000	220	2.53	0.215
Liu et al. [27]	ScAlN/AlN	4.02 × 4 × 0.551	1357.5	1	50	970	1.7	0.192
Liu et al. [27]	ScAlN/AlN	4.02 × 4 × 0.551	1284.25	1	95	756	10.74	1.214
Gablech et al. [28]	AlN	4 × 2 × 0.372	2520	1	67.56	900	3.1	1.04
He et al. [29]	AlN	13 × 14 × 0.402	160.6	1	240	NA	54.1	0.74
Elfrink et al. [30]	AlN	6.01 × 5 × 0.525	572.28	1	447	252	30	1.9
Zhao et al. [13]	AlN	11 × 12.12 × 0.502	230.4	1	70	NA	3.249	0.048
Yu et al. [12]	PZT	11 × 12.4 × 0.552	234.5	0.5	220	NA	66.75	3.55
Jackson et al. wide [10]	AlN	8.2 × 7 × 0.562	149	0.2	NA	124	3.07	2.38
Jackson et al. trapez. [10]	AlN	8 × 3.5 × 0.562	118	0.4	NA	131	1.15	0.46
Jackson et al. narrow [10]	AlN	7.5 × 1 × 0.562	97	0.4	NA	115	0.38	0.56
Jia et al. [15]	AlN	3.5 × 3.5 × 0.412	210	0.27	NA	NA	20.47	55.63

The results are decent and there is room for improvement. One way to improve the results by keeping the same design is to optimize the technological processes, especially the DRIE process in which the cantilevers are released. This could mean lower spacing between the cantilevers, hence a lower volume and a higher power density.

The design of a double array of cantilevers was based on the slight variation of the resonant frequencies with the variations in technological parameters resulting in a larger frequency bandwidth from which the device could harvest. A design of experiment (DOE) approach shows that the variation in the substrate thickness plays an important role in the variations in the resonant frequencies [31]. So, even if our device layer for the SOI wafer had a tolerance of +/−0.5 μm, this could translate to a significant variation in the resonant frequency. This, together with the high-quality factor of the individual cantilevers (Table 1), led to a significant difference in the phase of the cantilevers and we could not connect them in a more efficient way. This can be overcome by a proper design of the cantilevers

in order to compensate for these variations, design which implies an increased production cost. Another solution is to put a full-bridge rectifier for every cantilever, as shown by J.-Q. Liu et al. [11], but that means power losses for every additional piece of circuitry.

The power circuitry is an off-the-shelf solution. It offered the possibility for quick measurements at this stage. With an optimized geometry of the cantilevers and a custom design based on a specific application we can obtain better results.

Therefore, because of the technological drawbacks and a non-optimized power circuitry, we had to increase the acceleration in order to obtain a stabilized output voltage of 1.8 V.

The current results offer us the possibility to use this device for ultra-low-power applications, especially in the industrial field where we meet high acceleration sources and resonant frequencies in the few hundred of Hz range. It could be used to supply an ultra-low-power IoT device.

One of the most important advantages of this device is its potential for adaptability. Its design offers the possibility that the same device, with an area of 1 cm^2, could be used for multiple applications. With the proper optimization of the technological process, we can improve the number of usable cantilevers and we can group them according to the application. We can group all 20 items for a lower acceleration needs or we can group only a part of them for greater accelerations and multiple loads or even as spare cantilevers. We can also adapt for a more robust design with fewer but wider cantilevers.

For further studies we are working to reduce the resonant frequency of the device and the acceleration needed to obtain a useful stabilized output voltage by further optimizing the masks and process flow in order to obtain an array of cantilevers more suitable for ultra-low-power applications. Another plan is to mechanically clamp the cantilevers together to have the same resonant frequency but with the cost of frequency bandwidth.

5. Conclusions

An energy harvester with a double array of piezoelectric cantilevers (2 × 10) was fabricated and tested. The configuration of the lead-free piezoelectric cantilever consists of a Si substrate, a pair of Ti-Pt electrodes, a sputtered piezoelectric layer of 12% Sc-doped AlN with a thickness of 1000 nm, and a dielectric constant of ~13 and $e_{31,f}$ = 1.3 C/m^2.

Due to phase differences, only 10 cantilevers out of 20 were grouped together in order to harvest energy. By itself, the device (5p2s grouping) is able to generate a power of 2.53 μW for an optimal load resistance of 1 MΩ, at an excitation of 1 g and a resonant frequency of 465.3 Hz. In this case, the normalized power density of the device is 0.215 $\mu W/mm^3/g^2$, for the unpacked device and without the vibration volume. In comparison with similar devices, the results are decent, but they could be improved by further optimization of the technological processes or a redesign of the structure in order to take into consideration the high-quality factor of the individual cantilevers.

One of the focuses was to reach a stabilized voltage of 1.8 V. This was possible by increasing the excitation acceleration to 2 g and using the LTC3588-1 integrated circuit. The higher than usual value of the excitation acceleration makes this device suitable for industrial applications, like machine maintenance in factories.

Author Contributions: This paper was completed in collaboration between all authors. G.M. was involved in all aspects of the research. C.M., D.S. and J.Z. supervised all the aspects of the research. A.A. proposed the research theme and idea, co-designed and performed the theoretical analysis. B.F. and M.E. co-designed and conducted FEM simulations. C.B. and M.Z. co-designed and conducted the fabrication process. S.D., J.Z., I.S. and A.T. co-designed the testing experiments and co-worked on associated data collection and their interpretation. All authors have read and agreed to the published version of the manuscript.

Funding: This work was funded by the UEFISCDI during the M-era.Net project PiezoMEMS (2015–2018, Contract no. 12/2015) and led to another M-era.Net project funded by UEFISCDI, SmartEnergy

(2021–2024, Contract no. 240/2021). The work was also supported by the European Commission, through the HORIZON-WIDERA-2021-ACCESS-03 - Net4Air project, contract 101079455.

Data Availability Statement: The original contributions presented in the study are included in the article, further inquiries can be directed to the corresponding author/s.

Acknowledgments: The technological process was performed through IMT-MINAFAB and it was possible with assistance from PIEMACS Sàrl, Lausanne, Switzerland, for the piezoelectric layer. The ceramic packaging was provided by HIPOT-RR, Otočec, Slovenia.

Conflicts of Interest: Author Ion Stan was employed by the company Romelgen SRL. The remaining authors declare that the research was conducted in the absence of any commercial or financial relationships that could be construed as a potential conflict of interest.

References

1. Industrial Sensors Market Size, Share, Industry Report, Revenue Trends and Growth Drivers. Available online: https://www.marketsandmarkets.com/Market-Reports/industrial-sensor-market-108042398.html (accessed on 26 March 2024).
2. The European Green Deal—European Commission. Available online: https://commission.europa.eu/strategy-and-policy/priorities-2019-2024/european-green-deal_en (accessed on 26 March 2024).
3. Energy Harvesting System Market Size, Share, Industry Trends Forecast, Opportunities 2030. Available online: https://www.marketsandmarkets.com/Market-Reports/energy-harvesting-market-734.html (accessed on 26 March 2024).
4. Wang, L.; Yuan, F.G. Vibration Energy Harvesting by Magnetostrictive Material. *Smart Mater. Struct.* **2008**, *17*, 045009. https://doi.org/10.1088/0964-1726/17/4/045009.
5. Pan, C.T.; Liu, Z.H.; Chen, Y.C.; Chang, W.T.; Chen, Y.J. Study of Vibration-Induced Broadband Flexible Piezoelectric ZnO Micro-Harvester with Storage System. In Proceedings of the 2011 16th International Solid-State Sensors, Actuators and Microsystems Conference, Beijing, China, 5–9 June 2011; IEEE: Beijing, China, 2011; pp. 1669–1672.
6. Yi Li; Celik-Butler, Z.; Butler, D.P. A Piezoelectric Micro-Energy Harvester for Nanosensors. In Proceedings of the 2015 IEEE SENSORS, Busan, Republic of Korea, 1–4 November 2015; IEEE: Busan, Republic of Korea, 2015; pp. 1–4.
7. Kanno, I.; Ichida, T.; Adachi, K.; Kotera, H.; Shibata, K.; Mishima, T. Power-Generation Performance of Lead-Free (K,Na)NbO_3 Piezoelectric Thin-Film Energy Harvesters. *Sens. Actuators A Phys.* **2012**, *179*, 132–136. https://doi.org/10.1016/j.sna.2012.03.003.
8. Won, S.S.; Lee, J.; Venugopal, V.; Kim, D.-J.; Lee, J.; Kim, I.W.; Kingon, A.I.; Kim, S.-H. Lead-Free Mn-Doped ($K_{0.5}$,$Na_{0.5}$)NbO_3 Piezoelectric Thin Films for MEMS-Based Vibrational Energy Harvester Applications. *Appl. Phys. Lett.* **2016**, *108*, 232908. https://doi.org/10.1063/1.4953623.
9. Fei, C.; Liu, X.; Zhu, B.; Li, D.; Yang, X.; Yang, Y.; Zhou, Q. AlN Piezoelectric Thin Films for Energy Harvesting and Acoustic Devices. *Nano Energy* **2018**, *51*, 146–161. https://doi.org/10.1016/j.nanoen.2018.06.062.
10. Jackson, N.; O'Keeffe, R.; Waldron, F.; O'Neill, M.; Mathewson, A. Evaluation of Low-Acceleration MEMS Piezoelectric Energy Harvesting Devices. *Microsyst. Technol.* **2014**, *20*, 671–680. https://doi.org/10.1007/s00542-013-2006-6.
11. Liu, J.-Q.; Fang, H.-B.; Xu, Z.-Y.; Mao, X.-H.; Shen, X.-C.; Chen, D.; Liao, H.; Cai, B.-C. A MEMS-Based Piezoelectric Power Generator Array for Vibration Energy Harvesting. *Microelectron. J.* **2008**, *39*, 802–806. https://doi.org/10.1016/j.mejo.2007.12.017.
12. Yu, H.; Zhou, J.; Deng, L.; Wen, Z. A Vibration-Based MEMS Piezoelectric Energy Harvester and Power Conditioning Circuit. *Sensors* **2014**, *14*, 3323–3341. https://doi.org/10.3390/s140203323.
13. Zhao, X.; Shang, Z.; Luo, G.; Deng, L. A Vibration Energy Harvester Using AlN Piezoelectric Cantilever Array. *Microelectron. Eng.* **2015**, *142*, 47–51. https://doi.org/10.1016/j.mee.2015.07.006.
14. Barth, S.; Bartzsch, H.; Glöß, D.; Frach, P.; Modes, T.; Zywitzki, O.; Suchaneck, G.; Gerlach, G. Magnetron Sputtering of Piezoelectric AlN and AlScN Thin Films and Their Use in Energy Harvesting Applications. *Microsyst. Technol.* **2016**, *22*, 1613–1617. https://doi.org/10.1007/s00542-015-2787-x.
15. Jia, Y.; Seshia, A.A. Power Optimization by Mass Tuning for MEMS Piezoelectric Cantilever Vibration Energy Harvesting. *J. Microelectromech. Syst.* **2016**, *25*, 108–117. https://doi.org/10.1109/JMEMS.2015.2496346.
16. STM32L Series. Available online: http://www.st.com/en/microcontrollers/stm32l0-series.html?querycriteria=productId=SS1817 (accessed on).
17. MKW36A/35A/34A Data Sheet. Available online: https://www.nxp.com/docs/en/data-sheet/MKW36A512.pdf (accessed on).
18. MSP430 Ultra-Low-Power MCUs. Available online: http://www.ti.com/microcontrollers/msp430-ultra-low-power-mcus/products.html?pqs=paqs&familyid=342#~p3090=1.8V%20I/O (accessed on).
19. Williams, C.B.; Yates, R.B. Analysis Of A Micro-Electric Generator For Microsystems. In Proceedings of the International Solid-State Sensors and Actuators Conference—TRANSDUCERS '95, Stockholm, Sweden, 25–29 June 1995; IEEE: Stockholm, Sweden, 1995; Volume 1, pp. 369–372.
20. Matloub, R.; Hadad, M.; Mazzalai, A.; Chidambaram, N.; Moulard, G.; Sandu, C.S.; Metzger, T.; Muralt, P. Piezoelectric Al1−xScxN Thin Films: A Semiconductor Compatible Solution for Mechanical Energy Harvesting and Sensors. *Appl. Phys. Lett.* **2013**, *102*, 152903. https://doi.org/10.1063/1.4800231.
21. Priya, S. Criterion for Material Selection in Design of Bulk Piezoelectric Energy Harvesters. *IEEE Trans. Ultrason. Ferroelectr. Freq. Control* **2010**, *57*, 2610–2612. https://doi.org/10.1109/TUFFC.2010.1734.

22. Herdier, R.; Jenkins, D.; Remiens, D.; Dupont, M.; Osmont, D. A Silicon Cantilever Beam Structure for the Evaluation of D31, D33 and E31 Piezoelectric Coefficients of PZT Thin Films. In Proceedings of the 2007 Sixteenth IEEE International Symposium on the Applications of Ferroelectrics, Nara-City, Japan, 27–31 May 2007; pp. 725–727.
23. Belavic, D.; Muscalu, G.; Vojisavljevic, K.; Hodnik, M.; Kuscer, D.; Kos, T.; Pecnik, T.; Drnovsek, S.; Zajac, J.; Malic, B.; et al. Ceramic Packaging of PiezoMEMS Devices. In Proceedings of the 2017 21st European Microelectronics and Packaging Conference (EMPC) & Exhibition, Warsaw, Poland, 10–13 September 2017; IEEE: Warsaw, Poland, 2017; pp. 1–4.
24. TE Connectivity 820M1 Single Axis Condition Monitoring Accelerometer. Available online: https://www.te.com/commerce/DocumentDelivery/DDEController?Action=showdoc&DocId=Data+Sheet%7F820M1_Accelerometer%7FA4%7Fpdf%7FEnglish%7FENG_DS_820M1_Accelerometer_A4.pdf%7F20005838-00 (accessed on 26 March 2024).
25. Muscalu, G.; Firtat, B.; Dinulescu, S.; Moldovan, C.; Anghelescu, A.; Stan, I. Power Harvesting and Storage Circuit for a Double Array of Lead-Free Piezoelectric Cantilevers. In Proceedings of the 2018 International Semiconductor Conference (CAS), Sinaia, Romania, 10–12 October 2018; IEEE: Sinaia, Romania, 2018; pp. 321–324.
26. Linear Technology LTC3588-1—Nanopower Energy Harvesting Power Supply. Available online: https://www.analog.com/media/en/technical-documentation/data-sheets/35881fc.pdf (accessed on).
27. Liu, Y.; Hu, B.; Cai, Y.; Zhou, J.; Liu, W.; Tovstopyat, A.; Wu, G.; Sun, C. Design and Performance of ScAlN/AlN Trapezoidal Cantilever-Based MEMS Piezoelectric Energy Harvesters. *IEEE Trans. Electron. Devices* **2021**, *68*, 2971–2976. https://doi.org/10.1109/TED.2021.3072612.
28. Gablech, I.; Klempa, J.; Pekárek, J.; Vyroubal, P.; Hrabina, J.; Holá, M.; Kunz, J.; Brodský, J.; Neužil, P. Simple and Efficient AlN-Based Piezoelectric Energy Harvesters. *Micromachines* **2020**, *11*, 143. https://doi.org/10.3390/mi11020143.
29. He, X.; Li, D.; Zhou, H.; Hui, X.; Mu, X. Theoretical and Experimental Studies on MEMS Variable Cross-Section Cantilever Beam Based Piezoelectric Vibration Energy Harvester. *Micromachines* **2021**, *12*, 772. https://doi.org/10.3390/mi12070772.
30. Elfrink, R.; Kamel, T.M.; Goedbloed, M.; Matova, S.; Hohlfeld, D.; Van Andel, Y.; Van Schaijk, R. Vibration Energy Harvesting with Aluminum Nitride-Based Piezoelectric Devices. *J. Micromech. Microeng.* **2009**, *19*, 094005. https://doi.org/10.1088/0960-1317/19/9/094005.
31. {}Muscalu, G.-S.; Varachiu, N.; Firtat, B.; Dinulescu, S.; Tulbure, A.; Moldovan, C. Vibrational Energy Harvesting Devices for Structural Health Monitoring—Design Optimization. In Proceedings of the 2020 International Semiconductor Conference (CAS), Sinaia, Romania, 7 October 2020; IEEE: Sinaia, Romania, 2020; pp. 151–154.